Hot electron transport and a quantitative study of ballistic electron magnetic imaging on Co/Cu multilayers

A. Kaidatzis,* S. Rohart, A. Thiaville, and J. Miltat
Laboratoire de Physique des Solides, CNRS, Université Paris-Sud, UMR 8502, Bâtiment 510, F-91405 Orsay Cedex, France
(Received 8 July 2008; revised manuscript received 23 September 2008; published 24 November 2008)

We present a study of ballistic hot electron transport in Co/Cu/Co spin valves, using the ballistic electron emission microscope. By comparing samples with various Co thicknesses, we determine the hot electron attenuation length for both the minority- and majority-spin populations in the 1–2 eV energy range. Results are compared to recent calculations in order to qualitatively understand the hot electron attenuation lengths. Using the scanning ability of the microscope, we also present the imaging of different magnetic structures in the Co layers. In particular, we present a detailed study of the variation in 360° domain-wall morphology versus applied field. The images are compared with micromagnetic simulations. Good agreement is found that ultimately allows for an estimation of the resolution limits of this microscope.

DOI: 10.1103/PhysRevB.78.174426 PACS number(s): 75.60.Ch, 73.23.Ad, 75.47.Jn, 75.70.−i

I. INTRODUCTION

Among techniques for high-resolution magnetic imaging, ballistic electron emission microscopy[1–4] (BEEM) appears promising. The *magnetic* resolution of BEEM has never been estimated, although theoretical arguments and nonmagnetic BEEM measurements allow one to expect a resolution close to 1 nm.[5,6] The only technique with a similar or better resolution is the spin-polarized scanning-tunneling microscopy (SP-STM).[7,8] The advantage of BEEM is that it is sensitive to the thin-film volume as compared to SP-STM, which only probes surface magnetism. Moreover, BEEM does not necessarily need to be implemented in ultrahigh vacuum (UHV) since a capping layer may be used to protect the sample. Finally, BEEM is expected to be useful for samples that have been processed with standard nanofabrication techniques, which is impossible with SP-STM.

The principle of BEEM is to measure the transport of hot electrons emitted by the tip of a STM in a thin film or a multilayer.[5] In particular, it is possible to measure the hot electron attenuation length which describes their thermalization.[9–11] To distinguish between hot and thermalized electrons, the metallic layers are deposited on top of a semiconductor substrate, which provides an energy filter at the interface thanks to the Schottky barrier. For an injection energy higher than the Schottky-barrier energy, a fraction of the injected electrons cross the metallic stack ballistically (without scattering nor energy loss), reach the metal/semiconductor interface, and can enter the substrate according to momentum selection rules.[5,12] Using two contacts on the sample, one on the metallic layers and one in the substrate, it is possible to measure separately the hot and thermalized electron currents and characterize the yield of electrons (or transmission) into the semiconductor. BEEM offers a way to study locally (typically at the scale of 1 nm) the hot electron transport in the metal layers and also allows imaging by scanning the tip over the sample surface. Using a nonmagnetic tip, to obtain a magnetic contrast (MC), the metallic layers need to contain a "spin-valve" structure (two ferromagnetic layers separated by a nonmagnetic spacer).[3,4] The hot electron transmission depends on the relative magnetization orientation of the two ferromagnetic layers thanks to a difference in attenuation length between minority and majority electrons.[4,13–15] This difference leads to an intense contrast that may reach some hundreds of percent at room temperature.[16–18] The principle of BEEM magnetic imaging is analogous to the "polarizer-analyzer" concept in optics, with the "polarizer" being the ferromagnetic film (containing some domains) to be studied and the "analyzer" being a magnetically harder film with magnetization saturated along a given direction. In this case, the ballistic electron transmission map corresponds to the magnetic configuration of the polarizer layer.

During the course of BEEM development, two main topics need to be addressed. Spectroscopy measurements on samples with different thicknesses should allow determining the spin-dependent attenuation lengths in the ferromagnetic layer in order to understand the physics of hot electron attenuation in ferromagnetic metals. Then, magnetic imaging on model magnetic structures and simulations have to be performed in order to determine the limit of sensitivity and resolution of the microscope. In this paper, we address these two topics in Co/Cu/Co trilayers. In the first part, we present an extensive study of the hot electron attenuation versus sample thickness. The attenuation length variation versus energy allows a direct comparison with calculations. In the second part, we present an imaging study of the magnetization reversal in the two Co layers' stack, particularly when one layer contains a 360° domain wall (DW). We compare our results with micromagnetic simulations and try to determine precisely an upper bound to the microscope resolution.

II. EXPERIMENTAL DETAILS

BEEM measurements were performed at room temperature with a modified commercial scanning-tunneling microscope (STM) (Omicron STM-1).[19] The microscope was housed in an UHV chamber (base pressure $<4\times10^{-11}$ mbar), while externally attached coils supplied the magnetic field to the sample. STM tips were prepared from a 0.38-mm-diameter polycrystalline W wire by ac electrochemical etching in a KOH solution. STM images were pro-

cessed using the WSXM software.[20]

Commercially available P-doped *n*-type single side–polished Si(111) wafers (ρ=4–9 Ω cm) are used as substrates. Prior to deposition, an Ohmic contact is formed on the nonpolished back side of the wafers. For this purpose, the Si native oxide is removed with a buffered HF/NH_4F (7:1) solution, and a $Au_{0.99}Sb_{0.01}$(200 nm)/Cr(5 nm) bilayer is deposited by dc sputtering. The resistance between two AuSb/Cr/Si junctions is measured to be a few ohms at room temperature. Afterward, the wafers are diced into 5 $\times$5 mm^2 pieces. The hydrogenated Si(111) surface is prepared by means of wet chemical etching of the polished front side. The same buffered HF/NH_4F (7:1) solution is applied to remove the native oxide. A second anisotropic etching step is performed with a NH_4F (40%) solution, resulting in a surface decorated with (111) steps.[21]

Multilayers were deposited at room temperature in an independent UHV chamber using an e-gun evaporator. The base pressure of the evaporation unit was $<10^{-9}$ mbar, with a typical evaporation pressure of $\approx 10^{-8}$ mbar. The metal layers were evaporated through a copper foil mask so as to form a rectangular 1×0.5 mm^2 diode. High-purity (99.999%) metal pellets were used as source materials. The nominal deposition rate was 1.5 Å/s for each material and was monitored by a quartz-crystal microbalance and calibrated against profilometry and x-ray reflectivity measurements. The uncertainty in the evaluation of the thickness was estimated to be within $\pm$10%. The substrates were introduced into the UHV evaporation unit immediately after preparation. Initially a 7 nm Au layer was deposited to form a homogeneous Schottky contact (barrier height $>$0.8 eV and Schottky-diode ideality factor $n \leq 1.08$, as determined by current-voltage measurements). This Au/Si(111) structure provided a template on top of which the rest of the metal layer stack was deposited. The Au layer was polycrystalline with the crystallites' 10 to 20 nm in diameter, grown with the (111) orientation, as verified by STM and x-ray-diffraction measurements. Afterward, a 1.5 nm Cu seed layer was evaporated before the growth of single Co layers or Co/Cu/Co spin valves. For the present study, the spin valve consisted of two 1.8-nm-thick Co layers separated by a 6-nm-thick Cu spacer. Then, the film was protected with 1.5 nm Cu and 3 nm Au capping layers in order to allow for *ex situ* sample transfer. The rms roughness of the multilayer stacks was determined to be less than 1.5 nm by STM imaging.

III. HOT ELECTRON TRANSPORT

Hot electron transport in Co in the energy range of 1.0–2.0 eV above the Fermi level has been studied by BEEM spectroscopy. BEEM spectrum is a measure of the sample transmission versus tip voltage, with the tip kept at a fixed position. The sample transmission is defined as $T=I_B/I_T$, where I_B is the measured BEEM (hot electron) current and I_T is the injected tunnel current, which remains constant during acquisition. The energy distribution of the injected electrons can be described by an exponential decrease, starting at the Fermi level of the tip. For an energy decrease equal to 0.4 eV, typically, the tunneling probability decreases by $1/e$.[19]

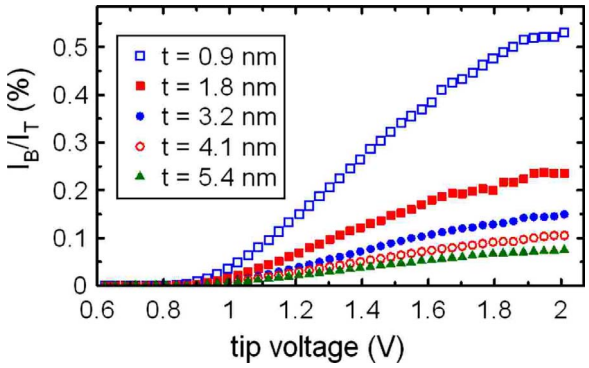

FIG. 1. (Color online) Hot electron transmission ($T=I_B/I_T$) versus tip voltage for single Co layers with various thicknesses (t). More than 100 spectra taken at several points of various 0.5 $\times$0.5 μm^2 scanning areas were averaged in each case. Injection current I_T=50 nA.

The hot electron transmission through samples containing single Co layers with various thicknesses was first studied as a function of the layer thickness (Fig. 1). Hot electron attenuation phenomena in the Au, Cu, and Co layers and at the Au/Cu, Cu/Co, and Au/Si interfaces all contribute to the transmission measured. The band splitting in Co has to be taken into account and two conduction channels are considered, one for the majority and one for the minority electrons.[22] The transmission of each conduction channel in Co is described by an exponential decay,[5] where λ_{maj} and λ_{min} are attenuation lengths for majority and minority electrons, respectively.[23,24] The hot electrons injected from the STM tip into the Au/Cu capping bilayer and then into the Co layer are not spin polarized, so that two initially equal spin populations are considered.[18] In the model described above, spin-dependent scattering at the Co/Cu interfaces is neglected following Ref. 13. The hot electron transmission through the metal/Si structure is thus described by

$$T = T_0\left[\frac{1}{2}\exp\left(-\frac{t}{\lambda_{maj}}\right)+\frac{1}{2}\exp\left(-\frac{t}{\lambda_{min}}\right)\right], \qquad (1)$$

where T_0 is the transmission for the total of the Au and Cu layers, including the Au/Cu, Au/Si, and Co/Cu interfaces, whereas the quantity in brackets describes the spin-dependent hot electron transport in the Co layer. By studying similar structures varying only the Co layer thickness t, it is possible to distinguish and study the attenuation of hot electrons in the Co layer since T_0 remains constant. The attenuation phenomena in the metal layers are energy dependent, so that T_0, λ_{maj}, and λ_{min} are also energy dependent.

In Fig. 2 the transmission at 1.5 V for the Co single-layer samples is plotted as a function of the Co layer thickness (similar graphs were obtained in the whole 1–2 V range). The transmission of a reference sample with no Co layer is also indicated. As a function of the thickness, two regimes are observed with different slopes: in the low–Co thickness regime, the transmission decreases faster than in the higher-thickness regime. As the minority electron attenuation length ($\approx$1 nm) is much shorter than the majority one,[4] after transport through a few attenuation lengths, minority electrons

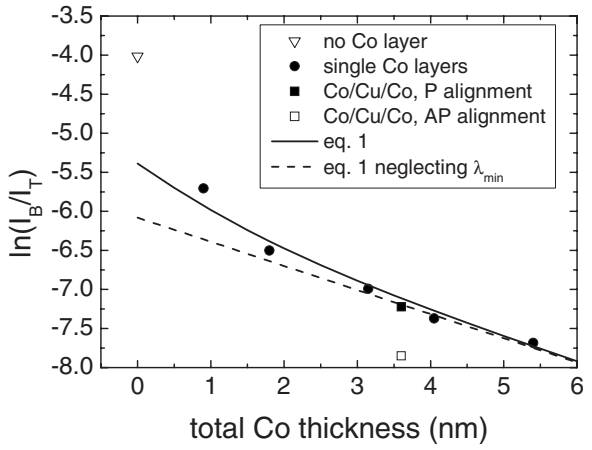

FIG. 2. Logarithm of the transmission versus total Co thickness for samples with Co single layers (disks) and Co/Cu/Co spin valves (squares) at 1.5 V. The transmission of a reference sample with no Co layer is indicated by a down triangle. The transmission of the spin-valve sample is measured for parallel (P; full square) and antiparallel (AP; open square) alignments of the two Co layers. Note that for this spin valve, the attenuation effect of the extra Cu layer (spacer) was calculated using an attenuation length in Cu of 20 nm and subtracted from the experimental data. The dashed line is a linear fit to the data for Co thicknesses larger than 3 nm and determines λ_{maj}. The continuous lines corresponds to Eq. (1) using λ_{maj} and λ_{min} values determined in the following.

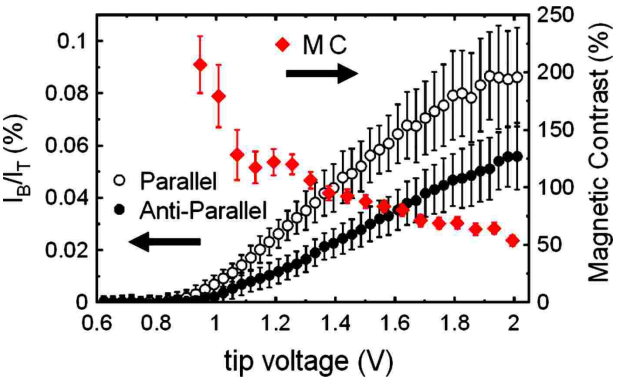

FIG. 3. (Color online) Hot electron transmission (I_B/I_T) versus tip voltage for the Co/Cu/Co sample measured for P and AP alignments of the two Co layers. More than 100 spectra taken at several 0.5×0.5 μm^2 scanning areas were averaged in each case. The error bars do not represent the measurement noise but account for the distribution of transmission from one area to another (Ref. 25). The magnetic contrast at room temperature is also shown [Eq. (4)]. Injection current I_T=50 nA.

have been almost totally scattered and the ballistic current contains almost only majority electrons. Then, for $t>3$ nm, the second exponential decay (corresponding to the minority electrons) can be neglected in Eq. (1), whereas the complete equation has to be used in order to fit all experimental data. A linear fit to the data in Fig. 2 for the high–Co thickness regime gives the value of the majority hot electron attenuation length (3.3 nm at 1.5 V). In principle, the whole thickness range could be fitted according to Eq. (1) in order to directly determine both λ_{maj} and λ_{min}. However, the lack of experimental data in the low-thickness regime makes the fitting process unreliable for the determination of λ_{min}.

From the linear fit for high layer thicknesses, T_0 can be determined and compared with the sample containing no Co layer. As shown in Fig. 2, T_0 is found to be four times smaller than the transmission of the reference sample. This indicates a strong scattering at the Co/Cu interfaces (considering equal attenuation at both Cu/Co and Co/Cu interfaces, 50% of the hot electrons are lost at each interface). As shown in Fig. 2, the transmission of the spin-valve sample is also in agreement with the single-layer samples, considering only two interfaces as already reported in Ref. 4 This surprising result probably means that only the first interface induces a 75% attenuation, while the other does not have any significant effect. The origin of this scattering is not clearly understood. Since no energy dependence was found (data not shown), elastic scattering due to defects and roughness at the interface appears more likely than a pure band-structure effect.

In order to determine λ_{min}, hot electron transport through a Co/Cu/Co spin valve with equal Co layer thicknesses (t) was studied as a function of the relative magnetization orientation of the two Co layers. By making use of the imaging capabilities of BEEM, P and AP aligned zones of the spin valve can be distinguished in zero field thanks to the presence of domains in both layers. Figure 3 shows spectra taken in each case for a spin valve with 1.8-nm-thick Co layers. The sample transmission in the P state is systematically higher than the transmission in the AP state. For a parallel alignment, majority (minority) electrons in the first layer are majority (minority) electrons as well in the second layer, so that the sample transmission is still given by Eq. (1), but taking into account as a thickness the total thickness of the two Co layers ($2t$):

$$T_P = T_0'\left[\frac{1}{2}\exp\left(-\frac{2t}{\lambda_{maj}}\right)+\frac{1}{2}\exp\left(-\frac{2t}{\lambda_{min}}\right)\right]. \quad (2)$$

Note that hot electron spin flip in Cu is neglected since the Cu thickness in much lower than the spin-relaxation length in Cu (Refs. 26 and 27) (more than 30 nm in the considered energy range[27]) so that equal attenuation lengths for each spin population are considered and that the polarization of the hot electron current in the spacer is constant. The attenuation due to the Cu spacer is included in $T_0'[T_0'=T_0\exp(-t_{Cu}/\lambda_{Cu})]$. For the antiparallel configuration, the majority (minority) electrons in the first layer are minority (majority) electrons in the second layer, so that the transmission is calculated to be

$$T_{AP} = T_0'\exp\left(-\frac{t}{\lambda_{maj}}\right)\exp\left(-\frac{t}{\lambda_{min}}\right). \quad (3)$$

The MC is defined as

$$MC = \frac{T_P - T_{AP}}{T_{AP}}. \quad (4)$$

The transmission of the Co/Cu/Co spin valve in the parallel state shown in Fig. 3 is in good agreement with previous measurements (see the black square in Fig. 2) if the

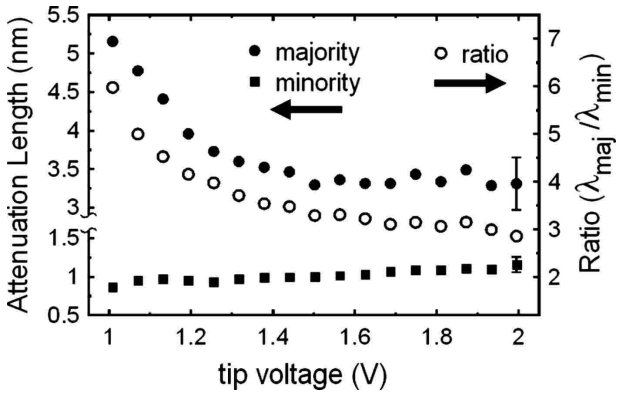

FIG. 4. Hot electron attenuation length for majority and minority electrons in Co at room temperature as a function of tip voltage. The error on the determination of the attenuation length is about 10% as indicated on the last dot of each curve.

attenuation due to the supplemental Cu spacer layer (6 nm thickness) is taken into account with an attenuation length of 20 nm in Cu.[28] The transmission in the antiparallel state is significantly lower (open square in Fig. 2). In Fig. 3, the magnetic contrast is found to decrease with electron energy, in accordance with previous studies,[14] from more than 200% just below 1.0 V to 50% at 2.0 V. Note that although the sample transmission is due to the metal layers and substrate, the magnetic contrast is only determined by the spin-dependent scattering occurring in the two Co layers. The fact that the MC value decreases with energy indicates that there is a significant energy dependence of λ_{maj} and λ_{min}.

Taking into account the λ_{maj} value found with the single–Co layer samples, λ_{min} can be deduced from the magnetic contrast. Figure 4 shows the values determined for the majority and minority electron attenuation lengths in the range of 1.0–2.0 V.

An important energy dependence of the attenuation length is observed. Moreover, keeping in mind that electron tunneling occurs as well in an energy range of few 100 meV below the tip voltage, the actual energy variation in the attenuation length is probably more important than what is shown in Fig. 4. λ_{maj} decreases from 5.2 to 3.3 nm in the range of 1.0–1.5 V and then remains relatively constant. On the contrary, λ_{min} increases from 0.9 to 1.2 nm throughout the whole energy range. The ratio of the two values decreases continuously from 6 to 2 in the range of 1.0–2.0 V, explaining the decrease in MC measured for the spin-valve sample. The values determined here are significantly higher than reported before,[4] potentially meaning higher film quality. More precisely, a similar energy dependence is found for λ_{min}, whereas a more clear variation is found for λ_{maj}.[4]

In order to interpret these results, we first recall that the attenuation length can be written as $\lambda(E)=v(E)\tau(E)$, where v is the electron velocity and τ is the electron lifetime, at energy E. The hot electron lifetime τ has two main contributions: the interaction between the hot electron and an electron below the Fermi level (interaction time $\tau_{e\text{-}e}$), and the interaction with defects (interaction time $\tau_{e\text{-}def}$).[29] They combine as $\tau^{-1}=\tau_{e\text{-}e}^{-1}+\tau_{e\text{-}def}^{-1}$.[29] The time $\tau_{e\text{-}e}$ is intrinsic to the material band structure, and thus can be calculated from first-principles calculation.[11,29,30] The calculation includes spin-flip and non-spin-flip electron-electron scatterings. It can also be estimated in the framework of the "phase-space model."[11] On the other hand, $\tau_{e\text{-}def}$ depends on the quality of the material and, being an elastic interaction, is not expected to vary with energy.[29] If the electron-defect interaction time is short, then defects dominate the lifetime, which becomes essentially constant. This could explain why, from a source of sample to another, the attenuation length and its energy dependence can change. Within this framework, a clear variation in the attenuation length is a sign that it is a true probe of the electron-electron interaction. The good agreement between our measurement for λ_{min} and that in Ref. 4 also fits well with this explanation, as λ_{min} is very short ($\approx$1 nm).

As there is no theoretical prediction for the attenuation length in Co, our results have to be compared with calculations performed for Fe and Ni.[11,30] In both cases the energy variations are quite similar to our result: in the energy range considered here, λ_{min} is almost constant, while λ_{maj} constantly decreases. This decrease is expected in the framework of the phase-space model[11] as the number of empty states between the Fermi level and the injection energy increases with injection energy for every metal. It is not straightforward to compare Co with Fe and Ni as these two last materials are surprisingly very different when dealing with hot electron attenuation.[11] For Ni, there is a strong lifetime asymmetry for hot electrons with energy of up to 3 eV, whereas for Fe, this asymmetry is rather weak. On the contrary, a strong hot electron velocity asymmetry has been calculated for Fe, which is not the case for Ni. As Co is in between Fe and Ni, the weight of these two contributions has to be determined precisely. Phase-space model calculations (not shown here) based on *ab initio* calculation of the fcc Co band structure predict a lifetime asymmetry τ_{maj}/τ_{min}, which decreases from 8.25 to 7.25 in the 1–2 eV energy range. However, as we do not know yet the velocity asymmetry, it is difficult to compare these results directly with our experimental data. More elaborate calculations are therefore required.

IV. BALLISTIC ELECTRON MAGNETIC IMAGING

By combining the BEEM ability of locally probing ballistic electron magnetotransport and the STM imaging capabilities, it is possible to create a map of the relative magnetization orientation of the two layers in the spin valve. For a parallel configuration the transmission is high, resulting in bright contrast, while for an antiparallel configuration the transmission is low, resulting in dark contrast.

The optimum energy for BEEM images can be estimated from Fig. 3. As shown in the spectra, a nonmagnetic noise due to the sample topography[25] superimposes onto the magnetic contrast. While the actual difference in transmission between the P and AP states increases with energy, taking into account error bars due to film structure, optimal contrast is expected in the 1.5–1.7 V range.

A. Comparison between BEEM and giant magnetoresistance

BEEM contrast bears a direct analogy with giant magnetoresistance (GMR) measurements since in the latter case the

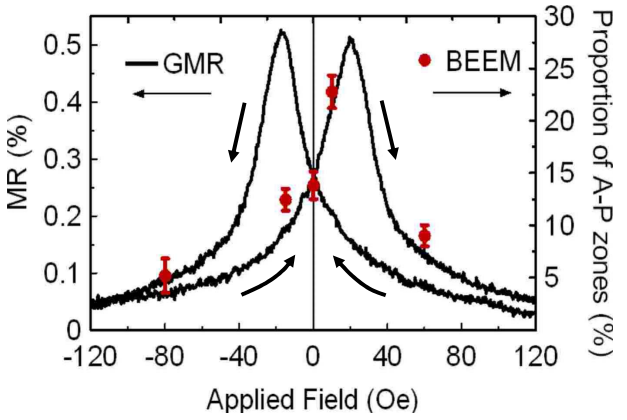

FIG. 5. (Color online) A current-in-plane GMR field cycle. The disks (in red) indicate the proportion of the anti-parallel aligned zones in the corresponding BEEM images (Fig. 6).

magnetoresistance (MR) value is a measure of the degree of magnetic collinearity of the spin valve. In Figs. 5 and 6, a GMR field cycle and a series of BEEM magnetic images in various fields applied on the film plane are compared. Due to experimental constraints, GMR and BEEM measurements were respectively taken from two different samples (10×10 mm^2 for GMR; 1×0.5 mm^2 for BEEM) but with identical Co(1.8 nm)/Cu (6 nm)/Co (1.8 nm) spin-valve stacks deposited simultaneously side by side. Figure 5 shows a GMR hysteresis cycle, where the maximum of the MR value is observed for a field of ≈ 20 Oe. Note also that magnetization reversal occurs in a large field range and that the signal saturation is only reached at ± 200 Oe.

Figure 6(a) shows the STM (surface topography) image corresponding to the BEEM image in Fig. 6(b). All other BEEM images were taken at the same position, as verified by the STM signal. In Fig. 6(b), a -80 Oe field is applied and the BEEM signal is almost homogeneously bright, with only a few dark zones indicating antiparallel orientation. As the applied field is increased to -10 Oe [Fig. 6(c)], the antiparallel aligned zones increase in area and increase even further at 0 Oe [Fig. 6(d)] and at +15 Oe [Fig. 6(e)]. Finally, at +60 Oe [Fig. 6(f)], the signal is almost homogeneously bright, corresponding again to parallel alignment. Note that in all images, small-scale signal fluctuations are apparent. They originate from the sample surface roughness and granular texture of the film as discussed above. It is evident from the topographic signal that the intense transmission depressions observed in the BEEM images do not originate from the film structure.

The disks on the GMR graph (Fig. 5) indicate the proportion of the antiparallel aligned zones as determined from the BEEM images (Fig. 6). The two scales have been adjusted so that the GMR and BEEM points coincide at zero field. There is rather good quantitative agreement between the two measurements, especially keeping in mind that the area probed by the GMR measurements (a few hundreds of μm^2; current-in-plane geometry) is much larger than for BEEM images (≈ 7 μm^2). It is interesting to notice that at +15 Oe, although the GMR signal corresponds to $\approx 80\%$ of its maximum value, BEEM shows an antiparallel configuration of the spin valve of less than 25%. This means that the GMR maximum does not correspond to an ideal antiparallel alignment and that a GMR signal more than four times higher could be

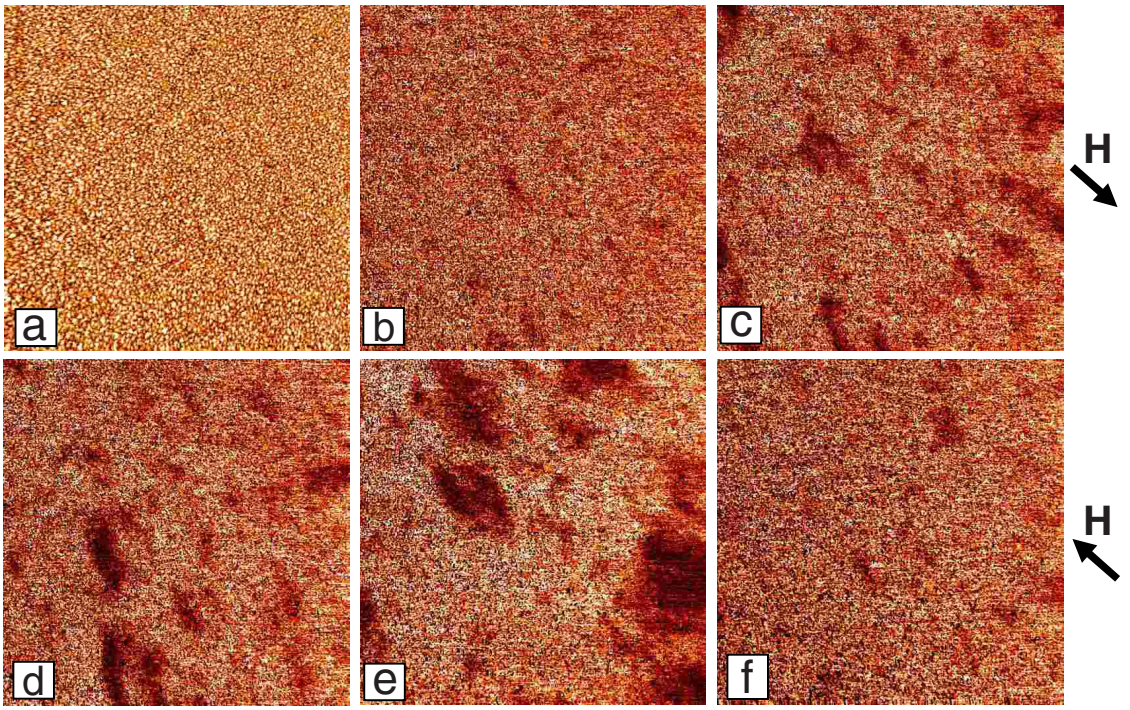

FIG. 6. (Color online) A series of BEEM magnetic images taken at a fixed position in a varying magnetic field applied on the film plane. (a) STM (surface topography) image corresponding to (b). Similar topography images were obtained for (c)–(f). [(b)–(f)] BEEM images respectively taken in fields of (b) -80, (c) -10, (d) 0, (e) +15, and (f) +60 Oe. Scan size was 2.6×2.6 μm^2. The tunnel parameters are $V_t = 1.6$ V and $I_t = 50$ nA. The color scale corresponds to transmission from 0.025% to 0.082%.

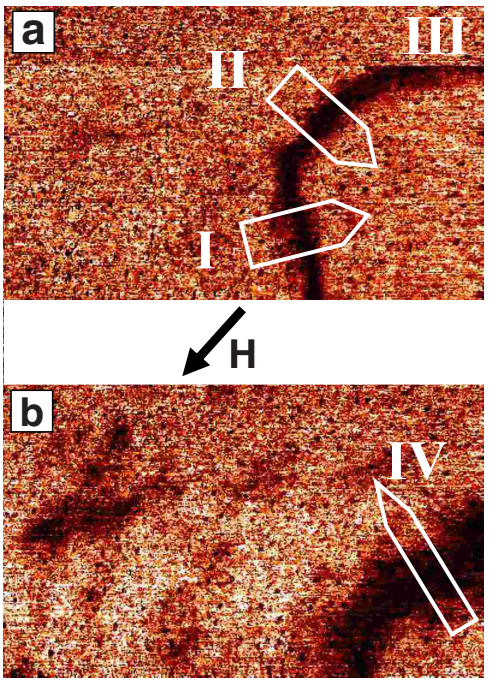

FIG. 7. (Color online) BEEM magnetic imaging of the same Co(1.8 nm)/Cu(6 nm)/Co(1.8 nm) spin valve as before. Images acquired at a fixed position in magnetic fields of (a) +100 and (b) +20 Oe applied on the film plane. The bright zones correspond to the saturated state of the spin valve, where both Co layers have magnetization parallel to the applied field. Before the acquisition of image (a), a field cycle was applied in the range of +200–+100 Oe. Image (b) was acquired immediately after image (a), with the applied field direction the same as in image (a). The boxes indicate the area and direction of the line profiles' averaging. Scan size: 2.4×1.5 μm^2. Tunneling parameters: $V_t=1.8$ V and $I_t=50$ nA. The color scale corresponds to transmission extending from 0.022% to 0.080%. The corresponding topographic images are not shown as they are identical to the image in Fig. 6(a).

achieved if the two magnetic layers were fully in antiparallel alignment, pointing out to the technological importance of fabricating spin valves with well-defined parallel and antiparallel configurations.

B. 360° domain walls

The high resolution of BEEM not only allows discussing the degree of magnetization collinearity of the spin valve or the size of the domains, but also allows observing of small details in the magnetic configurations, particularly the shape of the domain walls. In the following, we discuss the images of 360° domain walls.[31,32]

1. Experimental results

In Fig. 7(a) an image taken in a field of +100 Oe applied on the film plane is shown, while before acquisition several field cycles were applied in the 100–200 Oe range. The apparent dark feature corresponds to a 360° domain wall in one of the two Co layers.[33] This is supported by the fact that in a field of 100 Oe, both Co layers are almost saturated, as verified by magneto-optical Kerr effect (MOKE) (not shown) and GMR measurements (see Fig. 5). During magnetization reversal, 180° Néel domain walls sweep through the two Co films, and while passing over a structural defect they can be trapped and generate a 360° wall.[34] In Fig. 7(a) the defect pinning the domain wall is out of the scanning field and thus not apparent. In very thin films a 360° domain wall can only be eliminated in much higher fields than needed for moving regular 180° walls. Although there are no reports for the annihilation field in the case of thin Co films, values as high as 20 times the coercive field have been reported for (Co/NiFe/Co)/Cu multilayers.[35] For the Co embedded in Cu layers measured, a coercive field of ≈15 Oe is determined by MOKE magnetometry. Thus the 100 Oe applied field could be much smaller than the annihilation field.

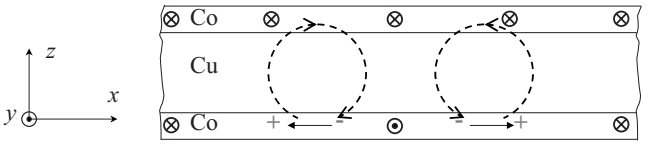

FIG. 8. Schematic 360° domain-wall structure in a two-layer sample, stabilized by a field aligned in the *y* direction. The magnetostatic charges in the domain-wall layer are indicated and the curved, dotted arrows sketch the stray field due to these charges.

The domain wall in Fig. 7(a) consists of three segments, labeled I–III in the figure, probably because of pinning at structural defects. The abrupt change in signal on the top of segment III does not correspond to an actual magnetic structure. Since the acquisition time of each image is several minutes and the scanning direction was from bottom to top, we may suppose that at this point the domain wall has been displaced under the influence of the applied field and temperature due to thermal activation. Immediately after, an image was taken in an applied field of +20 Oe, always at the same fixed position [Fig. 7(b)]. Dark signal patches have appeared, indicating nucleation of small domains as discussed before. The dark feature at the lower-right part corresponds to the 360° domain wall that has been indeed displaced (in that case, only one segment is observed and is labeled IV).

2. Micromagnetic modeling

In order to go beyond a simple description, a micromagnetic calculation of the structure of the 360° domain walls has been performed. In principle, the defects that make these domain walls exist should be taken into account (as in Ref. 32, for example). However, the BEEM images shown above are too small to reveal their position, and we do not know the defects' nature. Thus, as a first step, simple two-dimensional (2D) calculations in which the 360° domain wall is stabilized (compressed) by an applied field were performed. The wall was supposed to be infinitely long, and the calculation described the sample cross section perpendicular to the wall-extension direction (Fig. 8).The calculations used the 2D version of the OOMMF code,[36] with the magnetostatic calculation scheme that corresponds to an infinitely long sample. The micromagnetic parameters were those of bulk cobalt,

namely, $M_s=1400$ A/m, $A=30$ pJ/m, and $K=0$. The zero anisotropy was established by MOKE measurements, and corresponds to the polycrystalline nature of the cobalt layer. No exchange coupling was introduced between the two cobalt layers, as the copper spacer is too thick for oscillatory magnetic coupling to exist.[37] A mesh size of 2 nm was taken, so that the sample described by the computation is in fact Co (2 nm)/Cu (6 nm)/Co (2 nm). The extension of the calculation region in the x direction (see Fig. 8) was very large (10 μm). This way, magnetostatics can enforce that at the left and right x boundaries, the moments are along the y axis, even for low fields. A configuration containing the 360° domain wall in one layer and a saturated state in the reference layer was generated and relaxed under several y fields. With no pinning applied, the wall is eventually forced to leave the calculation region. In order to avoid this, a very large field $H_y=10^4$ Oe was applied to the central cell of the domain-wall layer only, in order to fix the magnetic direction of that cell.

The converged configurations show that the domain-wall layer, via magnetostatic coupling, influences the reference layer. Indeed, the magnetostatic charges present in the 360° domain-wall structure produce an x field in the other layer, which tilts magnetization toward the $\pm x$ direction (the so-called quasiwall structure[34]). Figure 9 displays the profiles of the m_y and m_x components of the magnetization unit vector $\vec{m}$ in both layers, at $H_y=-100$ Oe (the m_z component is suppressed by the demagnetizing field in each layer, and is below 0.03). The magnetization deviation due to the magnetostatic interaction is clearly seen in the profiles of m_x [Fig. 9(a)]: the reference layer has an m_x component with a sign opposite to that of the domain-wall layer, and a smaller magnitude. This deviation is the main effect of the magnetostatic coupling between the two magnetic layers. Indeed, the magnetization profile in the domain-wall layer is very close to that obtained when the structure is obtained with only the domain-wall layer (not shown). However, as displayed in Fig. 9(b), this deviation affects significantly the profile of the BEEM signal across the domain wall. The magnitude of the BEEM signal is proportional to the cosine of the angle between the local magnetization direction in the two layers, a law that results directly from the two currents' description with the assumption that the spins of electrons entering into a layer are measured (in the quantum-mechanical sense) along the local quantization axis. As the m_x have opposite signs in adjacent layers, the BEEM profile is always wider than the profile of the 360° domain wall itself.

If an isolated domain-wall layer is considered, analytic profiles can be calculated as drawn in Fig. 9. In the limit of a large y field, a one-dimensional (1D) model can indeed be built, with a magnetization confined to the x-y plane, described by an angle θ and no magnetostatic interaction. The energy of this model is the same as that entering the calculation of the 1D Bloch wall once the variable $\theta/2$ is considered, so that the domain-wall width parameter of this Bloch wall profile reads

$$\Delta = \sqrt{\frac{2A}{M_s B_y}}. \tag{5}$$

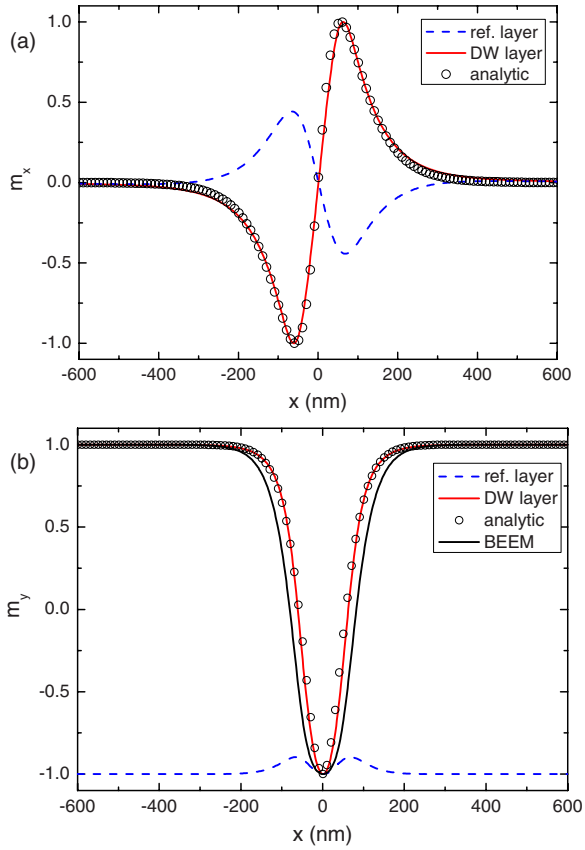

FIG. 9. (Color online) Profiles of the magnetization in both layers, for (a) the longitudinal component m_x and (b) the axial component m_y (b), in the case of an axial applied field $H_y=-10$ mT. The profiles in the domain-wall layer obtained with the analytical model are also superposed. In (b), the calculated BEEM contrast is also displayed. The FWHMs are 123.6, 115.4, and 163.2 nm for the numerical m_y in the DW layer, the analytical m_y, and the numerical BEEM signal, respectively.

At the large field considered (100 Oe), it appears that the numeric and analytic profiles are very close. More quantitatively, the full width at half maximum (FWHM) of the m_y component is expressed as $2\ln(1+\sqrt{2})\Delta$ in the analytic model. This prediction is ≈10% below the numerical results, in the field range of 10–300 Oe, a proof that magnetostatic effects are not so important in these ultrathin films. Thus, a fast increase in the 360° domain-wall width when the y field is reduced is predicted by the calculations.

3. Comparison between experiments and calculation

In order to compare experiments and calculations, line profiles were averaged along the indicated directions (Fig. 7). Since in Fig. 7(a) segment III is only partially imaged, we shall focus only on segments I, II, and IV. For segments II and IV, the applied field direction is parallel to the domain-wall axis, and for segment I the field direction is inclined at ≈55° with respect to the wall axis. First, the effect of the intensity of the applied field on the width of the domain wall is discussed. According to the experimental images, it is clear that the 360° domain wall is much larger at 20 Oe than at 100 Oe. In Fig. 10(a) the measured profile of segment II is

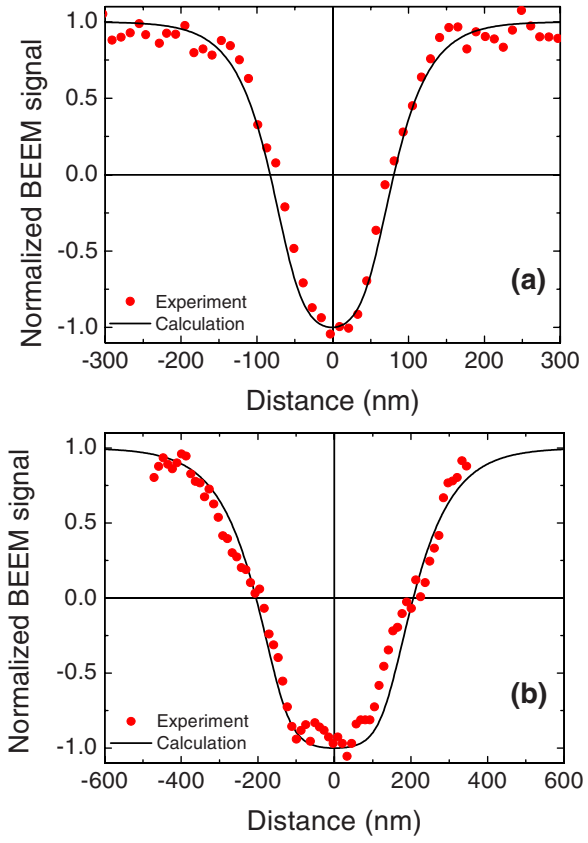

FIG. 10. (Color online) (a) Experimental and calculated domain-wall profiles in a 100 Oe field applied parallel to the wall axis [Fig. 7(a), segment II]. (b) Experimental and calculated domain-wall profiles in a 20 Oe field applied parallel to the wall axis [Fig. 7(b)]. The experimental profiles were averaged over several lines as indicated by the box in Fig. 7.

compared to the calculated profile of a 360° wall in a field of 100 Oe applied parallel to the wall axis. The FWHM of the wall is measured to be 160 nm, in good agreement with the calculated value, and the wall structure is symmetric. In Fig. 10(b) the measured profile of the wall (IV) in a field of 20 Oe [Fig. 7(b)] is compared to the corresponding calculated profile and shows also good overall agreement despite the possible presence of steps. In this case the wall has become wider (FWHM of 410 nm) due to the lower field, while the wall structure is always symmetric.

The structure of the wall is also affected by the applied field direction as can be observed in Fig. 7. For segment I the field is inclined by 55° from the domain-wall direction. It is noticeable that the transition region on the left side of the wall is wider than the one on the right side as displayed in Fig. 11. In the calculation, the effect of an additional x field was investigated in order to reproduce the misalignment between the domain wall and the external field. As can be seen from Fig. 8, the x field tends to favor one side of the wall at the expense of the other side. Thus, a dissymmetric domain-wall profile is created, and the symmetry that kept the domain wall at the center disappears (hence the localized pinning field in the calculation). The profiles corresponding to the fields applied in the experiment are superimposed onto experimental data in Fig. 11. This good match between images and micromagnetic calculations may even appear astonishing considering the noise present in the images. The conclusion is again that this noise has not a magnetic origin but, as pointed out before, is due to a distribution of fine structural defects.

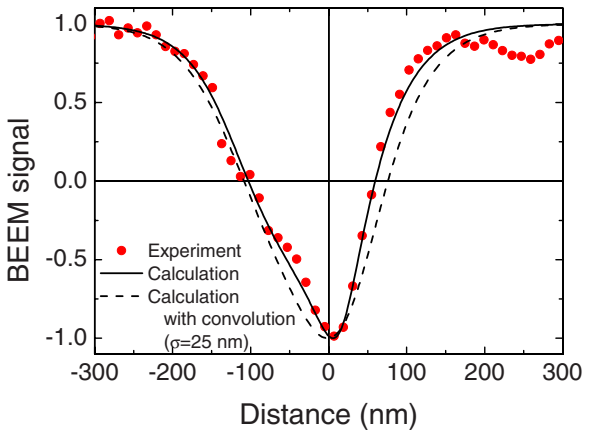

FIG. 11. (Color online) Experimental and calculated domain-wall profiles in an applied field of 100 Oe, with the direction of the field being inclined at 55° with respect to the domain-wall axis. The experimental profile was averaged over several lines as indicated by the box in Fig. 7. The continuous and dashed lines correspond to the calculation results without and with convolution, respectively.

The quantitative analysis of the BEEM magnetic contrast presented above allows us to discuss the magnetic resolution of the technique. In Ref. 33, the resolution of the images was estimated from 360° domain walls, calculating the transition-region width as the distance between the points where 20% and 80% of the maximum signal are reached. The authors have demonstrated a 28 nm resolution based on the sole signal analysis, irrespective of physical signal origin. The profile shown in Fig. 10(a) has a width on the order of a few tens of nanometer, which leads to a 80 nm resolution following the definition from Ref. 33. Since we do find very good agreement between experiments and calculations, we claim that this size corresponds to the actual magnetic structure size, and that it does not stem from a convolution effect due to the microscope resolution.

To go beyond and fix an upper bound to the resolution of the microscope, we consider the asymmetric calculated profile and calculate the effect of the convolution of the wall profile with a Gaussian distribution with variance σ. These convoluted profiles (scaled from maximum to minimum) are compared to the experimental asymmetric profile (Fig. 11). Good agreement is kept up to $\sigma=20$ nm. For higher σ, the asymmetric profile is distorted to such an extent that it would be difficult to distinguish between the symmetric and the asymmetric segments of the domain wall, a result ruled out by experiments. In this case, a convenient BEEM resolution definition would be the full width at half maximum of the Gaussian distribution, which is $2\sqrt{2\ln 2}\sigma$. According to this definition, the BEEM ability to resolve magnetic structures is better than ≈ 50 nm.

The simplest approximation of the BEEM process considers transport of hot free electrons in the metal base.[5] In the framework of this model, the nonmagnetic resolution of

BEEM is calculated to widen proportionally to the total film thickness, while it is a function as well of the electron energy.[5] The source of magnetic contrast in BEEM is the spin-dependent electron-electron scattering. As this only affects the magnitude of the collected current, we do not distinguish between the nonmagnetic and magnetic BEEM resolutions. The effect of the film thickness was shown in Ref. 38, where indeed the resolution was found to widen with the increase in the total film thickness. However, both the value of the resolution[39] and its degree of dependence on the film thickness cannot be explained by the model considered here.

In our case, the source of the spin-dependent scattering is in the Co layers. Thus, the total film thickness *above* these layers should be considered. In the case of the 360° domain wall, depending on whether the wall is in the upper or lower Co layer, the film thickness that should be considered is 4.5 or 10.5 nm, respectively. According to the model discussed above, the magnetic resolution (at 1.8 V tip voltage) is calculated to be 2 nm in the first case and 5 nm in the second case. These values are much lower than the measured one, supporting the claim that the measurement corresponds to the actual magnetic structure size.

V. CONCLUSION

In this paper, we have presented a study of the hot electron transport in Co/Cu/Co spin-valve samples using ballistic electron emission microscopy. We have determined the spin-dependent hot electron attenuation length in Co in the 1–2 eV energy range. We have shown that the attenuation length for majority electrons decreases versus energy, in opposition to previous results.[4] This tendency of our results is quite similar to the prediction for Fe and Ni.[11] Theoretical calculations for Co would be quite interesting to confirm our result.

We have also shown imaging of magnetic structures in the Co layers using the scanning ability of the microscope. In the case of the image of 360° domain walls, we have compared experimental results with calculations, and reached good agreement. These results show that the resolution of the microscope is very good, better than 50 nm. However, this value only corresponds to an upper bound for the resolution. Magnetic configurations on smaller scale such as narrower domain walls are needed to find the true resolving limit of BEEM magnetic imaging

ACKNOWLEDGMENTS

We gratefully acknowledge the help of J. Ferré for magneto-optical characterization, M. Aprili for e-beam evaporation and the loan of his deposition setup, and A. Gloter for band-structure calculations. Financial support was provided by C'Nano Île de France STCalib project). A.K. received funding from the EC Marie Curie host training site Emergent CondMatPhys (Grant No. MEST-CT-2004-514307).

*kaidatzis@lps.u-psud.fr

[1] W. J. Kaiser and L. D. Bell, Phys. Rev. Lett. **60**, 1406 (1988).
[2] L. D. Bell and W. J. Kaiser, Phys. Rev. Lett. **61**, 2368 (1988).
[3] W. H. Rippard and R. A. Buhrman, Appl. Phys. Lett. **75**, 1001 (1999).
[4] W. H. Rippard and R. A. Buhrman, Phys. Rev. Lett. **84**, 971 (2000).
[5] M. Prietsch, Phys. Rep. **253**, 163 (1995).
[6] H. Sirringhaus, E. Y. Lee, and H. von Känel, Phys. Rev. Lett. **74**, 3999 (1995).
[7] R. Wiesendanger, H.-J. Güntherodt, G. Güntherodt, R. J. Gambino, and R. Ruf, Phys. Rev. Lett. **65**, 247 (1990).
[8] M. Bode, J. Phys.: Condens. Matter **66**, 523 (2003).
[9] L. D. Bell, Phys. Rev. Lett. **77**, 3893 (1996).
[10] V. Narayanamurti and M. Kozhevnikov, Phys. Rep. **349**, 447 (2001).
[11] V. P. Zhukov, E. V. Chulkov, and P. M. Echenique, Phys. Rev. B **73**, 125105 (2006).
[12] F. J. Garcia-Vidal, P. L. de Andres, and F. Flores, Phys. Rev. Lett. **76**, 807 (1996).
[13] R. Vlutters, O. M. J. van tErve, S. D. Kim, R. Jansen, and J. C. Lodder, Phys. Rev. Lett. **88**, 027202 (2001).
[14] E. Haq, T. Banerjee, M. H. Siekman, J. C. Lodder, and R. Jansen, Appl. Phys. Lett. **88**, 242501 (2006).
[15] T. Banerjee, J. C. Lodder, and R. Jansen, Phys. Rev. B **76**, 140407(R) (2007).
[16] D. J. Monsma, J. C. Lodder, T. J. A. Popma, and B. Dieny, Phys. Rev. Lett. **74**, 5260 (1995).
[17] S. van Dijken, X. Jiang, and S. S. P. Parkin, Appl. Phys. Lett. **83**, 951 (2003).
[18] R. Heer, J. Smoliner, J. Bornemeier, and H. Bruckl, Appl. Phys. Lett. **85**, 4388 (2004).
[19] A. Thiaville, F. Caud, C. Vouille, and J. Miltat, Eur. Phys. J. B **55**, 29 (2007).
[20] I. Horcas, R. Fernàndez, J. M. Gómez-Rodríguez, J. Colchero, J. Gómez-Herrero and A. M. Baro, Rev. Sci. Instrum. **78**, 013705 (2007).
[21] P. Dumas, Y. J. Chabal, and P. Jakob, Surf. Sci. **269-270**, 867 (1992).
[22] D. R. Penn, S. P. Apell, and S. M. Girvin, Phys. Rev. Lett. **55**, 518 (1985).
[23] D. P. Pappas, K.-P. Kamper, B. P. Miller, H. Hopster, D. E. Fowler, C. R. Brundle, A. C. Luntz, and Z.-X. Shen, Phys. Rev. Lett. **66**, 504 (1991).
[24] J. C. Gröbli, D. Oberli, and F. Meier, Phys. Rev. B **52**, R13095 (1995).
[25] The error bars in Fig. 3 correspond to the standard deviation of the measurement. However, they mainly indicate the local variations in transmission because of the surface roughness, and to a lesser extent the actual noise of the measurement. Since the films are polycrystalline, electrons that tunnel from the tip to the edges of a grain will be injected into the film at an angle inclined with respect to the normal of the plane of the metal/semiconductor interface. This causes the ballistic electrons to travel a longer path and thus attenuate more until they reach the metal/semiconductor interface. Moreover, their highly off-normal momentum direction causes high reflection at the metal/semiconductor interface, reducing even further the ballistic cur-

rent measured (Ref. 40). Spectroscopy curves acquired on polycrystalline films show an overall transmission that scales inversely with the injection angle. Those local variations in the BEEM transmission because of the surface structure are always present, and during imaging give rise to a contrast related to surface topography (Ref. 41).

[26] A. C. Perrella, P. G. Mather, and R. A. Buhrman, J. Appl. Phys. **98**, 093713 (2005).

[27] V. P. Zhukov, E. V. Chulkov, and P. M. Echenique, Phys. Status Solidi A **205**, 1296 (2008).

[28] The Cu attenuation length has not yet been determined. However, the lifetime calculation in Ref. 29 and the band structure let us suppose that it is high and similar to that for Au [30–15 nm in the 1–2 eV energy range (Ref. 11)].

[29] E. V. Chulkov, A. G. Borisov, J. P. Gauyacq, D. Sánchez-Portal, V. M. Silkin, V. P. Zhukov, and P. M. Echenique, Chem. Rev. (Washington, D.C.) **106**, 4160 (2006).

[30] V. P. Zhukov, E. V. Chulkov, and P. M. Echenique, Phys. Rev. Lett. **93**, 096401 (2004).

[31] L. J. Heyderman, H. Niedoba, H. O. Gupta, and I. B. Puchalska, J. Magn. Magn. Mater. **96**, 125 (1991).

[32] T. Schrefl, J. Fidler, and M. Zehetmayer, J. Appl. Phys. **87**, 5517 (2000).

[33] E. Haq, T. Banerjee, M. H. Siekman, J. C. Lodder, and R. Jansen, Appl. Phys. Lett. **86**, 082502 (2005).

[34] A. Hubert and R. Schäfer, *Magnetic Domains* (Springer, Berlin, 1998).

[35] L. J. Heyderman, J. N. Chapman, and S. S. P. Parkin, J. Magn. Magn. Mater. **138**, 344 (1994).

[36] M. J. Donahue and D. G. Porter, , National Institute of Standards and Technology Interagency Report No. NISTIR 6376, 1999 (unpublished).

[37] S. S. P. Parkin, R. Bhadra, and K. P. Roche, Phys. Rev. Lett. **66**, 2152 (1991).

[38] C. Tivarus, J. P. Pelz, M. K. Hudait, and S. A. Ringel, Appl. Phys. Lett. **87**, 182105 (2005).

[39] The resolution in this case, as measured by the authors, is found to be significantly wider than in other studies (Ref. 6). However, a different interpretation of the data (for a similar study, see Ref. 42 could attribute the observations to effects not related to BEEM and, thus, to BEEM resolution.

[40] A. Bauer, M. T. Cuberes, M. Prietsch, and G. Kaindl, Phys. Rev. Lett. **71**, 149 (1993).

[41] C. A. Ventrice, V. P. LaBella, G. Ramaswamy, H.-P. Yu, and L. J. Schowalter, Phys. Rev. B **53**, 3952 (1996).

[42] D. Rakoczy, G. Strasser, and J. Smoliner, Appl. Phys. Lett. **86**, 202112 (2005).